NUMERICAL SIMULATIONS OF A HEAVY-LIFT EVTOL

Timotheos Chronis, The University of Manchester, Manchester, UK
Dima Usov, The University of Manchester, Manchester, UK
Antonio Filippone, The University of Manchester, Manchester, UK
Tao Zhang, The University of Leicester, Leicester, UK
George Barakos, The University of Glasgow, Glasgow, UK

Abstract

Simulations of a multi-rotor eVTOL aircraft at high disk-loading condition were undertaken in hovering flight using a viscous vortex particle method combined with a lifting-line blade model. Constant-source panels were used to introduce the influence of the airframe in the solution. Comparisons with CFD results revealed that the vortex-particle solver was capable of predicting the time-averaged propeller thrusts to within 6%. Additionally, the primary (1/rev) blade thrust variations due to the inter-propeller interactions were well-captured. However smaller-scale variations and interactions between the propellers and wings were not resolved to the same extent.

1. NOTATION

Symbols	Description
A_{ij}	Vortex panel influence coefficient
c	Panel mean chord length, m
C_{ij}	Source panel influence coefficient
$\boldsymbol{dF}$	Panel inviscid force vector, N
$\boldsymbol{dl}$	Panel quarter chord segment, m
K	Velocity kernel, m/s
$\hat{\boldsymbol{n}}$	Panel unit normal vector, m
$\boldsymbol{r}$	Distance vector, m
R	Propeller radius, m
t	Time, s
$\boldsymbol{\alpha}$	Particle vorticity strength vector, m^3/s
$\boldsymbol{\omega}$	Vorticity, 1/s
$\mathbf{u}$	Velocity, m/s
$\mathbf{u}_{\boldsymbol{k}}$	Panel kinematic velocity, m/s
$\mathbf{u_s}$	Velocity induced by source panels, m/s
$\mathbf{u_v}$	Velocity induced by vortex panels, m/s
$\mathbf{u_w}$	Velocity induced by wake particles, m/s
$\mathbf{x}$	Position vector, m
T	Thrust, N
Γ	Circulation, m^2/s
ν	Kinematic viscosity, m^2/s
ρ	Air density, kg/m^3
σ	Particle core radius, m
σ	Panel source strength, m/s
ϕ	Inflow angle, deg
ψ	Blade azimuth angle, deg
Ω	Propeller speed of rotation, rad/s

2. INTRODUCTION

In the field of Advanced Air Mobility (AAM), a large variety of electric vertical take-off and landing (eVTOL) concepts have been offered as private or low-capacity transportation. Yet, there are barriers to their adoption in such a role, including traffic management solutions, noise annoyance, and high operating costs (Ref. 1). Recent socioeconomic studies (Refs 2,3) have found that high-capacity regional AAM operations would generate considerably more profits, with greater public acceptance. Heavy-lift eVTOL designs, such as the GKN Skybus concept presented in Ref.4, are hence of particular research interest. The heavy weight leads to high disk loadings, and subsequently, strong aerodynamic interference across rotors, wings, and airframe. These have been identified in previous high-fidelity CFD analyses in both hover and forward flight conditions (Refs 4,5). While high-fidelity CFD methods can resolve accurate flow details, aerodynamic loadings, and acoustic emissions, their computational cost may still exceed the affordability of many routine design tasks. It is then an interesting question to understand whether faster predictive methods are capable of resolving the interactional flow physics with reasonable accuracy.

In recent years, there has been considerable effort invested by multiple institutions into developing the vortex particle method as a robust and reliable tool for predicting wake mixing and the effects of lifting-surface interactions, e.g., Refs 6-8. The main advantage of this method is the ability to resolve blade forces and primary aerodynamic interactions at a much lower computational cost than high-fidelity solvers. This makes parametric design investigations much more feasible. Zanotti et al. (Ref. 9) demonstrated that, in the case of a full tiltrotor model during hover and transition flight, a vortex particle wake coupled with a Morino-like boundary element method and a nonlinear lifting line, can provide qualitatively similar predictions to CFD for blade loads and flow field velocities.

Previous works have dealt with the initial sizing, blade optimisation, and forward flight aeroacoustics of the heavy-lift eVTOL layout using an URANS-based CFD solver, with consideration for the wake interactions between the fixed wings and propellers in two-, four- and six-propeller configurations (Refs 4,10). This was followed by CFD studies which established the aeroacoustic performance of the optimized geometry in hover and highlighted the overall improvements compared to the original baseline (Ref. 5). The latest study investigated the feathering and windmilling of a redundant propeller in forward flight and the effect of this propeller's wake on downstream elements (Ref. 11).

The wealth of CFD data available for the heavy-lift eVTOL presents an opportunity to assess the capability of alternative, more efficient computational methods in resolving the various aerodynamic interactions present between the propellers and lifting surfaces. Specifically, the objective of this study is a code-to-code comparison of the prediction of the unsteady blade loads, where the CFD solution will be compared to that from a vortex particle code, VorTeX. In this code, the vortex particle method is coupled with a lifting line model for fast predictions of the lifting surface loads under the influence of their wakes and other surfaces.

3. NUMERICAL METHODS

3.1. Vortex Particle Method

The code VorTeX was developed for the solution of rotary wing flows based on the vortex particle method (VPM). The VPM solves the vorticity form of the incompressible Navier-Stokes equations (Equation 1) in a Lagrangian frame of reference by discretizing the flow field into regularized vortex elements, called vortons or vortex particles.

$$\frac{D}{Dt}\boldsymbol{\omega} = (\boldsymbol{\omega}\cdot\nabla)\mathbf{u} + \nu\nabla^2\boldsymbol{\omega} \quad (1)$$

The method is efficient in the sense that only regions of the flow with non-zero vorticity need to be discretised, hence it is well suited for vortex-dominated flows such as in the wakes of fixed and rotary wings. The code was written in MATLAB, with performance-critical functions converted to C code using MATLAB's Mex file format.

The vorticity field, $\boldsymbol{\omega}$, is approximated from Equation 2 as the sum over all particles, which are defined by a vorticity strength, $\boldsymbol{\alpha}_p$, and by a core size, σ_p. The latter desingularises the influence of each particle and enables the simulation to proceed without numerically blowing up.

$$\boldsymbol{\omega}(\mathbf{x},t) \approx \sum_p^N \boldsymbol{\alpha}_p(t)\zeta_\sigma\left(\mathbf{x}-\mathbf{x}_p(t)\right) \quad (2)$$

The function ζ_σ is selected to be a Gaussian radial basis function. The velocity field, $\mathbf{u}$, is obtained as the induction from all vortex elements via the Biot-Savart law with a regularised kernel, $K_\sigma = g_\sigma K$, with a smoothing radius that corresponds to the core size of the particles:

$$\mathbf{u}(\mathbf{x},t) = \sum_p g_\sigma\left(\mathbf{x}-\mathbf{x}_p(t)\right)K\left(\mathbf{x}-\mathbf{x}_p(\boldsymbol{t})\right)\times\boldsymbol{\alpha}_p$$

with $K(\boldsymbol{r}) = -\frac{r}{4\pi r^3}$ (3)

The core radius is selected such that an initial overlap between neighbouring particles of at least one core radius is maintained for numerical stability.

The particle evolution equations follow the reformulation of Alvarez et al. (Ref. 6), which avoids the assumption of constant particle core size in favour of a variable core scheme that locally conserves the momentum of vortex tubes as they are subjected to stretching:

$$\frac{d}{dt}\mathbf{x}_p = \mathbf{u}(\mathbf{x}_p) \quad (4)$$

$$\frac{d}{dt}\boldsymbol{\alpha}_p = \left(\boldsymbol{\alpha}_p \cdot \nabla\right)\mathbf{u}\left(\mathbf{x}_p\right) - \frac{3}{5}\left\{\left[\left(\boldsymbol{\alpha}_p \cdot \nabla\right)\mathbf{u}\left(\mathbf{x}_p\right)\right] \cdot \widehat{\boldsymbol{\alpha}}_p\right\}\widehat{\boldsymbol{\alpha}}_p + \left.\frac{d\boldsymbol{\alpha}_p}{dt}\right|_{visc} \quad (5)$$

$$\frac{d}{dt}\sigma_p = -\frac{1}{5}\frac{\sigma_p}{\|\alpha\|_p}\left[\left(\boldsymbol{\alpha}_p \cdot \nabla\right)\mathbf{u}\left(\mathbf{x}_p\right)\right] \cdot \widehat{\boldsymbol{\alpha}}_p \quad (6)$$

The particle strength exchange scheme of Degond and MasGallic (Ref. 12) is used to model the effects of viscous diffusion in the final term of Equation 5, although for the flows in this study, the effect was found to be negligible. The relaxation scheme by Pedrizetti (Ref. 13) is used to realign the particles with the curl of the local velocity and reinforce the solenoidality of the vorticity field.

3.2. Lifting Line

To obtain the blade loads, a linear lifting line is solved by discretizing the lifting surfaces into quadrilateral vortex panels. The velocity induced by their constituent vortex filaments is also obtained via the Biot-Savart law. The bound circulation distribution is obtained by enforcing the flow-tangency condition at the centroid of the bound vortex panels, described as the method of influence coefficients in Katz and Plotkin (Ref. 14). This is done concurrently with the solution of the source terms, as described in Section 3.3. The Prandtl-Glauert compressibility correction is also applied to the circulation. The coupling with the VPM is achieved by shedding the bound circulation into the wake in the form of a row of temporary panels, the filaments of which are then converted into particles to be evolved in the following time step. The shed filament coincident with the trailing edge of the bound vortex panels is also preserved into the next time step as an element contributing to the wake-induced velocity so that the bound circulation is updated correctly.

Once the circulations are determined, the steady and unsteady inviscid forces on each panel are computed using the vectorised Kutta-Joukowski formulation from Ref. 15:

$$\boldsymbol{dF} = \rho\Gamma(\mathbf{u} \times \boldsymbol{dl}) + \rho c\frac{\partial\Gamma}{\partial t}\widehat{\boldsymbol{n}}$$

where $\boldsymbol{dF}$ is the force on the panel, ρ is the air density, Γ is the panel circulation strength, $\mathbf{u}$ is the local velocity vector calculated in the middle of the quarter-chord segment, $\boldsymbol{dl}$, c is the mean chord of the panel, and $\widehat{\boldsymbol{n}}$ is the unit normal vector of the panel.

3.3. Boundary Element Method

Fuselages and other non-lifting bodies are represented by constant-source panels, the strengths of which are determined by solving a Neumann boundary problem. The flow-tangency condition at the centroids of each source or vortex panel can be expressed in terms of the kinematic velocity of the panel, $\mathbf{u}_k$, the velocity induced by the free wake particles, $\mathbf{u}_w$, and the influence of all other source and vortex panels, $\mathbf{u}_s$ and $\mathbf{u}_v$:

$$(\mathbf{u}_s + \mathbf{u}_v + \mathbf{u}_w - \mathbf{u}_k) \cdot \widehat{\boldsymbol{n}} = \mathbf{0} \quad (7)$$

By moving the wake and kinematic velocities to the right-hand side, a linear system of equations can then be obtained, which is solved for the source and circulation strengths, σ and Γ, respectively. This is shown in Equation 8, with notation borrowed from Tugnoli et al. (Ref. 7), where the matrices C_{ss}, C_{vs} contain the influence coefficients of source panels on all source and vortex panels respectively, and the matrices A_{sv}, A_{vv} contain the influence coefficients of vortex panels on all source and vortex panels.

Applying Equation 7 for source panel i:

$$(\mathbf{u}_s + \mathbf{u}_v)_i \cdot \widehat{\boldsymbol{n}}_i = -(\mathbf{u}_w - \mathbf{u}_k)_i \cdot \widehat{\boldsymbol{n}}_i$$

$$\sum_k^{N_s} C_{ik}\sigma_k + \sum_m^{N_v} A_{im}\Gamma_m = RHS_i$$

Hence for all source panels: $[C_{ss}\ A_{sv}]\binom{\sigma}{\Gamma} = b_s$

Applying Equation 7 for vortex panel j:

$$(\mathbf{u}_s + \mathbf{u}_v)_j \cdot \widehat{\boldsymbol{n}}_j = -(\mathbf{u}_w - \mathbf{u}_k)_j \cdot \widehat{\boldsymbol{n}}_j$$

$$\sum_k^{N_s} C_{jk}\sigma_k + \sum_m^{N_v} A_{jm}\Gamma_m = RHS_j$$

Hence for all vortex panels: $[C_{vs}\ A_{vv}]\binom{\sigma}{\Gamma} = b_v$

The combined system of equations is then:

$$\begin{bmatrix} C_{ss} & A_{sv} \\ C_{vs} & A_{vv} \end{bmatrix}\binom{\sigma}{\Gamma} = \binom{b_s}{b_v} \quad (8)$$

Solution of this linear system is performed using the Matlab backslash ("\") operator, which computes the inverse of the matrix of influence coefficients using LU factorisation.

3.4. CFD Solution

The reference data, against which the VPM solution is compared, was obtained using the well-established Helicopter Multi-Block 3 (HMB3) framework (Refs

16,17). HMB3 solves the unsteady Reynolds averaged Navier-Stokes equations in integral form using the Arbitrary Lagrangian Eulerian formulation for time-dependent domains, which may include moving boundaries. The Navier-Stokes equations are discretised using a cell-centred finite volume approach on a multi-block, structured grid. The 3rd order Monotone Upstream-centred Schemes for Conservation Laws (MUSCL) approach was used to provide high-order accuracy in space. The chimera/overset grid method was used.

4. GEOMETRY AND OPERATING CONDITIONS

The baseline C1 configuration of the heavy-lift eVTOL was considered in hovering conditions out of ground effect, as described in Refs 4,11. This consisted of six propellers mounted on wing tips in a hexagonal configuration, as shown in Figure 1.

The optimized blade geometry from Ref. 4 was used with a radius, R, of 3.25 m. The blade twist was modified by adding to the geometric twist the zero-lift angle of attack due to the airfoil camber at the approximate operating Reynolds and Mach number. The propeller pitch was set to 23.8 degrees at 0.75 radius and the angular speed was set to 338 RPM. The starboard-side propellers are shown in the results that follow.

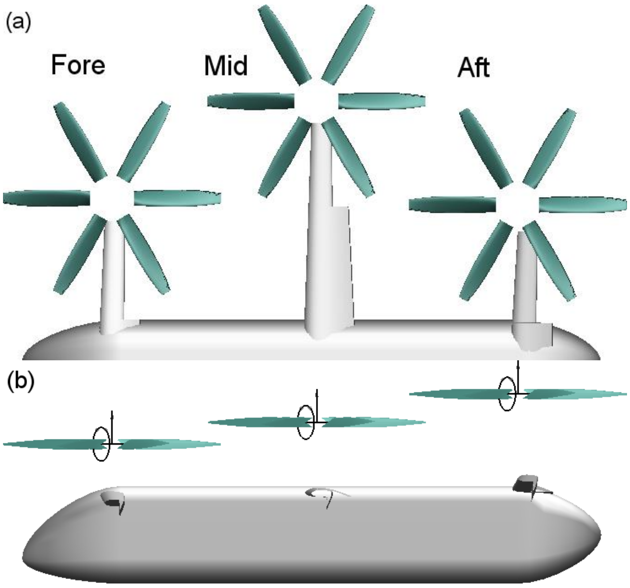

Figure 1: (a) Top and (b) side view of the aircraft geometry.

5. RESULTS

VPM simulations were run for two cases: one where only the propellers were modelled (PO) and one also considering the influence of the wings (PW). To economise on the total number of surface panels, the fuselage was not modelled in either case, as its influence on the blade loads was not expected to be significant due to the high disk loadings and relatively large lateral separation of the propellers. That said, we acknowledge that the absence of a fuselage may lead to a misrepresentation of the fountain-flow recirculation region known to occur in the centre of such a propeller arrangement.

A symmetric boundary condition along the longitudinal plane of the aircraft was enforced, implemented using the method of mirror images (Refs 14,18). A time step corresponding to 5 degrees of azimuth rotation was selected, with a spanwise discretization of 30 panels. A cosine distribution of panels was used to better resolve the tip regions of the blades. The front and aft wings consisted of 1200 panels each, while the mid wing consisted of 1500 panels.

Although the CFD results are accepted as the ground truth for the purposes of the following comparisons, it is important to keep in mind that there is no guarantee for their accuracy, even with a solver that has been well-validated.

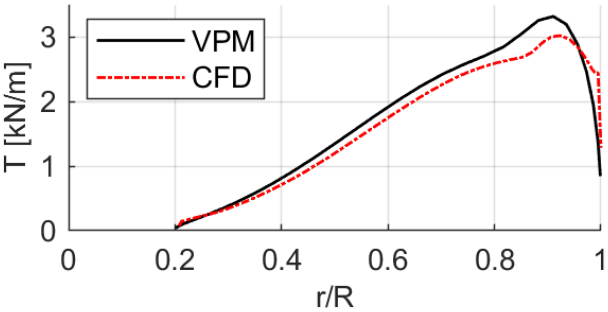

Figure 2: Blade thrust distributions for an isolated propeller.

5.1. Time-Averaged Loads

Table 1: Mean propeller thrusts for the VPM and CFD solutions.

Case	$\bar{T}$ [kN] Fore	$\bar{T}$ [kN] Mid	$\bar{T}$ [kN] Aft
VPM-PO	27.4	27.8	27.6
VPM-PW	27.7	27.7	27.5
CFD	26.2	26.5	26.2

Table 1 shows a comparison of the predicted thrusts for each propeller. Even from the PO case, the propeller thrusts predicted by the VPM solution display decent agreement with the CFD results, with a difference in mean values below 6%. The inclusion of the wings lead to an increase in mean thrust of 0.3 kN for

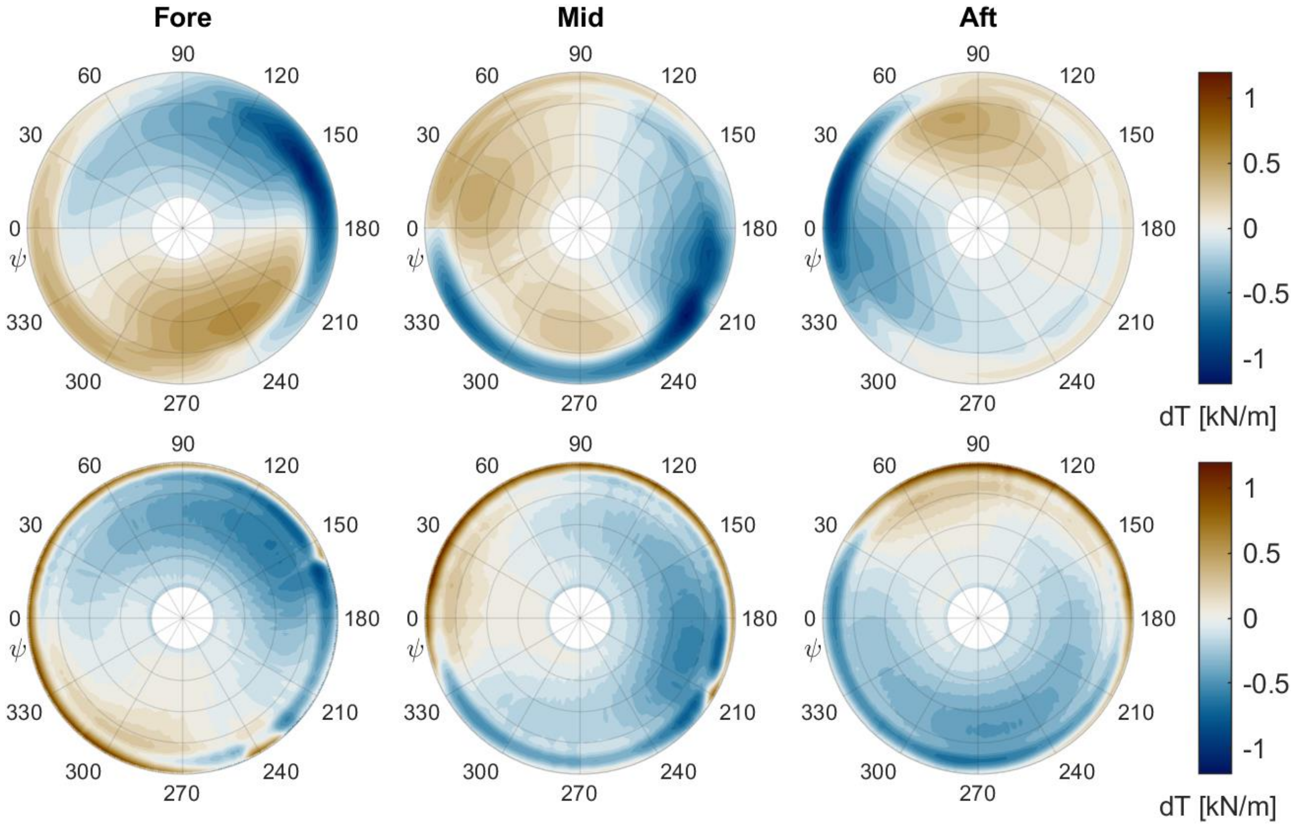

Figure 3: Change in thrust from an isolated propeller, for the VPM-PW (top) and the CFD (bottom) solution. Positive values indicate an increase compared to the isolated case. Zero azimuth is defined at the front of the disk.

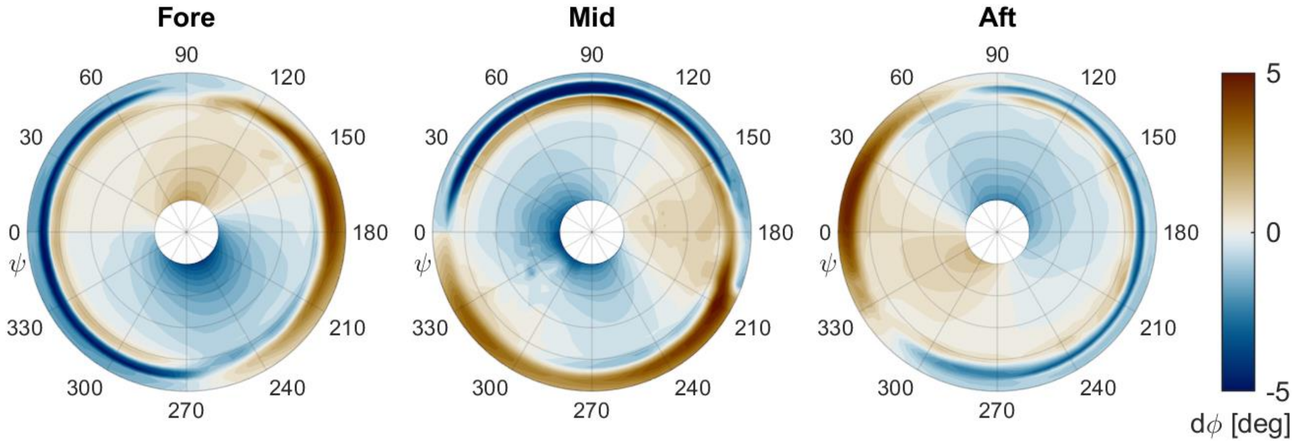

Figure 4: Change in inflow angle from the isolated case for the VPM-PW solution. Positive values indicate an increase compared to the isolated case.

the fore propeller and a reduction of 0.1 kN for the mid and aft propellers.

5.2. Blade Loads

Firstly, a comparison of the thrust distributions for the blade of an isolated propeller is shown in Figure 2. At the same propeller pitch, the VPM solver overpredicted the integrated blade thrust compared to the CFD solution by 7.1%. While the two solutions agreed well over most of the blade span, differences are highlighted near the tip, with the VPM solution having a higher spanwise gradient in the region outboard of the thrust peak. The location of maximum thrust is also slightly inboard compared to the CFD solution. The lifting-line model is unable to account for complex 3D effects around the tip since it only considers the blade as a zero-thickness surface with a prescribed shedding point at the trailing edge.

Figure 3 shows contours of the thrust distributions for all propellers relative to the thrust of an isolated propeller. The CFD solution predicted an overall increase in the tip thrust in the outside regions of the propeller formation, which was present in the VPM solution, albeit smaller in magnitude. The regions of reduced thrust on the inside of the formation were also generally well-captured by the VPM, particularly for the mid propeller, which saw most of its influences from the other propellers rather than from the airframe.

The thrust of a single blade from each propeller over a revolution is plotted in Figure 5. It is clear that the overall 1/rev variation was well-captured for all three propellers. However, with the exception of the mid propeller, the secondary variations in thrust due to blade-blade (B2B) and blade-wing (B2W) interactions were poorly resolved. The presence and nature of these secondary interactions was identified via a Fourier analysis of the CFD results, as described in the previous paper (Ref. 5). The addition of the wings made a small difference to the thrust variation of the fore propeller, but was otherwise negligible.

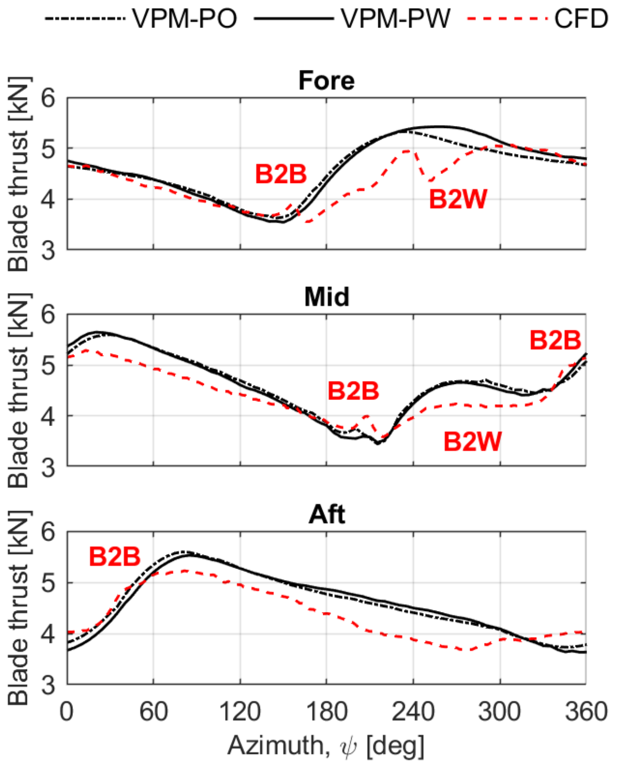

Figure 5: Averaged single blade thrusts over a revolution. Blade-blade and blade-wing interactions are annotated as B2B and B2W respectively.

It is worth noting that the VPM solutions did not reach a fully periodic state, with each blade having a slightly different thrust variation over its revolution. Averaging over the blades resulted in some of the pertinent B2B interactions becoming attenuated, together with other perturbations. This was especially the case for the mid propeller where the thrust doublet at 200 degrees was noted to have almost double the amplitude for blades two and five compared to the average shown in Figure 5.

5.3. Wake Characteristics

The propeller wakes are visualised in Figure 6 for both the VPM and the CFD solutions. Near the propellers, the wakes exhibit similar coherent vortical structures trailed from the blade tips. As these tip vortices are convected downstream, instabilities are amplified and they eventually collapse to form a region of unstructured vorticity. It is noted that the region where tip vortices become destabilised but remain coherent extends slightly further downstream in the VPM solution than in the CFD solution.

On the other hand, as the wake evolves and vortex filaments become stretched and distorted, the density of particles is insufficient to accurately represent small-scale features of the vortex breakdown and instead the particle field devolves into a disorganised state. This behaviour could be improved with a remeshing scheme, such as particle splitting, to ensure that core overlap is maintained. However, it is not critical for correct load predictions.

Regarding the wake interaction with the airframe, some spanwise propagation along the wings is observed in the VPM case, however not to the extent of the CFD solution, where the vortices meet in the centre of the fuselage.

6. DISCUSSION

As the blade interactions were described in detail in Ref. 5, this discussion will instead focus on the discrepancies between the VPM and CFD solutions. Considering the contours of Figure 4, for the fore propeller, the region of higher thrust in the tip region from 60 to 160 degrees is absent in the VPM results. A similar result is observed for the mid propeller in the outboard region from 150 to 210 degrees, although some of the thrust at 210 degrees is recovered, leading to the small feature observed in the integrated blade loads of Figure 5.

The largest discrepancy in thrust for the fore propeller is in the azimuth range from 180 to 240 degrees,

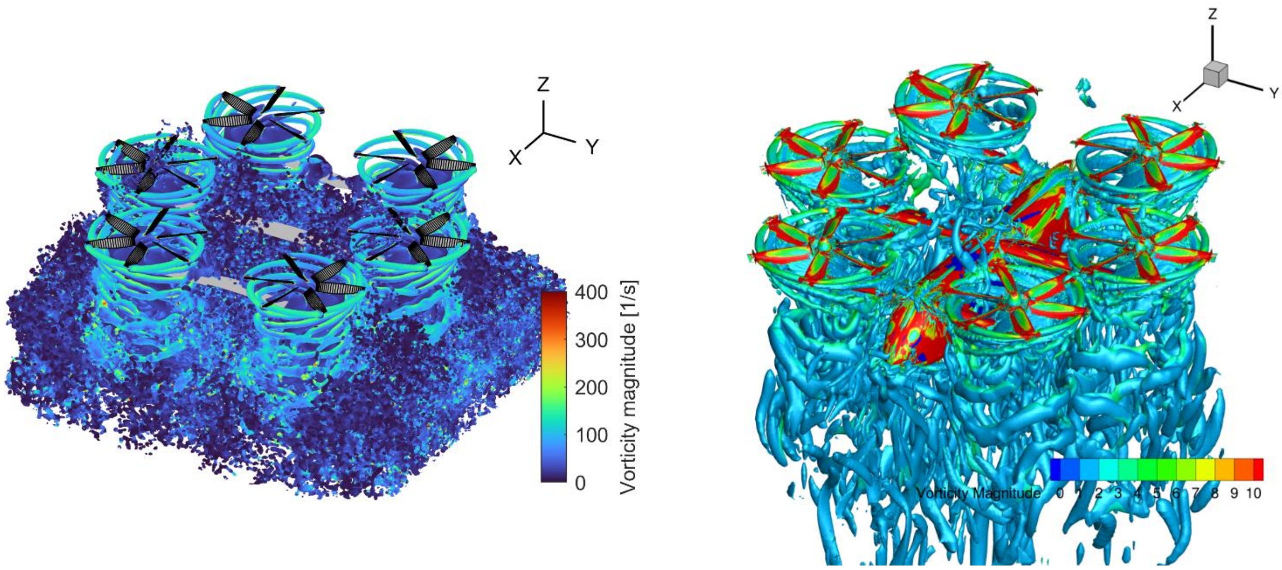

Figure 6: Isosurfaces of Q-criterion for the VPM-PW solution (left) and the CFD solution (right). The right panel is reproduced from Ref. 5.

where the VPM model predicts a thrust of 0.5-1 kN per blade higher compared to the CFD result. From the contours, this increase appears to be towards the midspan of the blade. A similar observation is made for the aft propeller. The absence of fuselage and associated flow recirculation could be a contributing factor to the thrusts being on average higher on the inboard side of the fore and aft propellers for the VPM solution. Some differences are observed in this regard in the wake visualisations of Figure 6 that point towards this being the case.

The contours of the change in inflow angle, shown in Figure 4, indicate that there is an increased downwash on the inside of the formation of propellers, which correlates well with the reduction in tip thrust in those azimuth ranges. This is consistent with other results on compact multirotor configurations in hover (Ref 19,20).

The effect of the inclusion of the wings on the blade loads is very small. The biggest change is noted for the fore rotor, at azimuth angles 240-300 degrees. The increase in thrust resembles a wing thickness loading effect and appears with a delay of about 30 degrees compared to the CFD prediction, which shows an unsteady doublet instead. This is perhaps a direct limitation of the representation of the wing surface using source terms only. The inclusion of vortex or doublet terms for the surface panels could yield improved results, as seen in similar works (e.g. Ref. 7).

Due to the lack of elements with non-zero circulation, surface loads cannot be obtained for the wings themselves. This presents a limitation when trying to determine the download on the wings, which from the CFD was estimated at a combined 6% of the MTOW of the aircraft, with an additional 6% from the fuselage – a total of 1680 kg. Further, the lack of a vortex shedding mechanism, combined with the inviscid flow assumption inherent to the method, leads to spuriously low pressures on the trailing edges of the wing flaps, as the flow is forced to remain attached around the sharp edges.

In terms of computational time, the VPM solution took approximately 4,200 CPU hours, with around 500,000 particles in the final time step of the simulation. This represents a significant saving compared to the approximately 100,000 combined CPU hours for the CFD solution. This could be improved further with acceleration algorithms, such as the fast multipole method (FMM), which can be used to reduce the computational complexity of the N particle interactions to a theoretical O(N), plus computational overhead (Ref. 21). Furthermore, modification of the simulated geometry would only require the adjustment of a few generating parameters, obviating the need for any time-consuming mesh generation. This makes the solution method well suited to optimisation tasks and parametric investigations.

7. CONCLUSIONS

In this study, a solver based on the vortex particle method and the lifting line was used to predict the blade loads of a heavy-lift multirotor eVTOL aircraft in hovering conditions. A constant-source boundary-element method was used to introduce the influence of the wings on the blade loads. The results were compared to previous CFD simulations of the same configuration, with the following key conclusions:

1. The VPM solver predicted the mean propeller thrusts to within 6% of the CFD solution, for a computational cost between 10-100 times smaller.
2. The primary 1/rev variations of the blade loads were well-predicted by the VPM solver for all propellers, however, some of the smaller blade-blade interactions, which were confined to the tip regions of the blades, were not resolved.
3. The method remains better suited to analysis in the preliminary design stage, where its computational efficiency, ease of setup and relatively good accuracy would enable fast iterations of design configurations.

Author contact:

Timotheos Chronis; timotheos-georgios.chronis@manchester.ac.uk

Dima Usov; dmitrij.usov@manchester.ac.uk

Antonio Filippone; a.filippone@manchester.ac.uk

Tao Zhang; tz77@leicester.ac.uk

George Barakos; george.barakos@glasgow.ac.uk

8. ACKNOWLEDGMENTS

This research was partly funded by EPSRC Engineering and Physical Sciences Research Council Grant EP/W010119/1 Greener Aviation with Advanced Propulsion Systems (GAAPS). Travel was funded by the UK Chapter of the Vertical Flight Society. The authors wish to acknowledge the assistance given by Research IT and the use of the Computational Shared Facility at The University of Manchester. This work used colour maps by Fabio Crameri (Ref. 22).

9. REFERENCES

1 A. Filippone and G. Barakos, "Rotorcraft Systems for Urban Air Mobility: A Reality Check," *The Aeronautical Journal,* vol. 125, no. 1283, pp. 3-21, 2021. doi.org/10.1017/aer.2020.52.

2 EASA, "Study on the Societal Acceptance of Urban Air Mobility in Europe," EASA, 2021. https://www.easa.europa.eu/sites/default/files/dfu/uam-full-report.pdf.

3 PWC, "Advanced Air Mobility: UK Economic Impact Study," PWC, 2023. https://www.pwc.co.uk/intelligent-digital/drones/uk-economic-aam-report-2023.pdf.

4 T. Zhang, G. N. Barakos, Furqan and M. Foster, "Multi-fidelity aerodynamic design and analysis of propellers for a heavy-lift eVTOL," *Aerospace Science and Technology,* vol. 135, 2023. https://doi.org/10.1016/j.ast.2023.108185.

5 T. Zhang, G. N. Barakos, A. Filippone and Furqan, "High-fidelity Aero-acoustic Evaluations of a Heavy-lift eVTOL in Hover," *Journal of Sound and Vibration,* vol. 584, p. 118453, 2024. doi.org/10.1016/j.jsv.2024.118453.

6 E. J. Alvarez, J. Mehr and A. Ning, "FLOWUnsteady: An Interactional Aerodynamics Solver for Multirotor Aircraft and Wind Energy," in *AIAA Aviation 2022 Forum*, Reston, VA, 2022. https://doi.org/10.2514/6.2022-3218.

7 M. Tugnoli, D. Montagnani, M. Syal, G. Droandi and A. Zanotti, "Mid-fidelity Approach to Aerodynamic Simulations of Unconventional VTOL Aircraft Configurations," *Aerospace Science and Technology,* vol. 115, p. 106804, 2021. https://doi.org/10.1016/j.ast.2021.106804.

8 V. Proulx-Cabana, M. T. Nguyen, S. Prothin, G. Michon and E. Laurendeau, "A Hybrid Non-Linear Unsteady Vortex Lattice-Vortex Particle Method for Rotor Blades Aerodynamic Simulations," *Fluids,* vol. 7, no. 2, 2022. https://doi.org/10.3390/fluids7020081.

9 A. Zanotti, A. Savino, M. Palazzi, M. Tugnoli and V. Muscarello, "Assessment of a Mid-Fidelity Numerical Approach for the Investigation of Tiltrotor Aerodynamics,"

Applied Sciences, vol. 11, no. 8, p. 3385, 2021. https://doi.org/10.3390/app11083385.

10 T. Zhang, G. N. Barakos, Furqan and M. Foster, "Multi-Fidelity Aerodynamic and Acoustic Design and Analysis of a Heavy-Lift eVTOL," in *48th European Rotorcraft Forum*, Winterthur, 2022.

11 T. Zhang, G. N. Barakos and Furqan, "On the Aerodynamic Performance of Redundant Propellers for Multi-Rotor eVTOL in Cruise," *Aerospace Science and Technology,* vol. 145, 2024. https://doi.org/10.1016/j.ast.2023.108846.

12 P. Degond and S. Mas-Gallic, "The Weighted Particle Method for Convection-Diffusion Equations. Part 1: The Case of an Isotropic Viscosity," *Mathematics of Computation,* vol. 53, no. 188, pp. 485-507, 1989. https://doi.org/10.2307/2008716.

13 G. Pedrizzetti, "Insight into Singular Vortex Flows," *Fluid Dynamics Research,* vol. 10, no. 2, pp. 101-115, 1992. https://doi.org/10.1016/0169-5983(92)90011-K.

14 J. Katz and A. Plotkin, Low-Speed Aerodynamics, 2nd ed., New York: Cambridge University Press, 2001.

15 O. Sugar-Gabor, "A General Numerical Unsteady Non-Linear Lifting Line Model for Engineering Aerodynamics Studies," *The Aeronautical Journal,* vol. 122, no. 1254, pp. 1199-1228, 2018. doi.org/10.1017/aer.2018.57.

16 R. Steijl, G. Barakos and K. Badcock, "A framework for CFD analysis of helicopter rotors in hover and forward flight," *International Journal for Numerical Methods in Fluids,* vol. 51, no. 8, pp. 819-847, 2006. doi.org/10.1002/fld.1086.

17 M. Biava, M. Woodgate and G. N. Barakos, "Fully Implicit Discrete-Adjoint Methods for Rotorcraft Applications," *AIAA,* vol. 54, no. 2, pp. 735-749, 2016. doi.org/10.2514/1.J054006.

18 J. Zhao and C. He, "Physics-Based Modeling of Viscous Ground Effect for Rotorcraft Applications," *Journal of the American Helicopter Society,* vol. 60, no. 3, p. 032006, 2015. doi.org/10.4050/JAHS.60.032006.

19 D. Shukla and N. Komerath, "Multirotor Drone Aerodynamic Interaction Investigation," *Drones,* vol. 2, no. 43, 2018. doi.org/10.3390/drones2040043.

20 S. Miesner, M. Keßler, E. Krämer and U. Schäferlein, "Investigation of Near Ground Effects in Hover Flight for the Multi-Rotor Aircraft Volocopter-2X," in *VFS 76th Annual Forum & Technology Display*, Virtual, 2020. doi.org/10.4050/F-0076-2020-16409.

21 H. Cheng, L. Greengard and V. Rokhlin, "A Fast Adaptive Multipole Algorithm in Three Dimensions," *Journal of Computational Physics,* vol. 155, no. 2, pp. 468-498, 1999. doi.org/10.1006/jcph.1999.6355.

22 F. Crameri, "Scientific colour maps (7.0.1)," doi.org/10.5281/zenodo.5501399.

10. CLASSIFICATION & COPYRIGHT